ACS APPLIED MATERIALS & INTERFACES

Research Article

www.acsami.org

On the Performances of Cu_xO-TiO_2 (x = 1, 2) Nanomaterials As Innovative Anodes for Thin Film Lithium Batteries

D. Barreca,*[,†] G. Carraro,[‡] A. Gasparotto,[‡] C. Maccato,[‡] M. Cruz-Yusta,[#] J. L. Gómez-Camer,[#] J. Morales,[#] C. Sada,[§] and L. Sánchez*[,#]

[†]CNR-ISTM and INSTM, Department of Chemistry, Padova University, 35131 Padova, Italy

[‡]Department of Chemistry, Padova University and INSTM, 35131 Padova, Italy

[#]Departamento de Química Inorgánica e Ingeniería Química, Universidad de Córdoba, 14071 Córdoba, Spain

[§]Department of Physics and Astronomy and CNISM, Padova University, 35131 Padova, Italy

Supporting Information

ABSTRACT: Cu_xO-TiO_2 (x = 1, 2) nanomaterials are synthesized on polycrystalline Ti substrates by a convenient chemical vapor deposition (CVD) approach, based on the initial growth of a Cu_xO matrix (at 400 and 550 °C for x = 1 and 2, respectively) and the subsequent overdispersion of TiO_2 at 400 °C. All CVD processes are carried out in an oxygen atmosphere saturated with water vapor. The obtained systems are investigated by means of glancing incidence X-ray diffraction (GIXRD), X-ray photoelectron spectroscopy (XPS), secondary ion mass spectrometry (SIMS), field emission-scanning electron microscopy (FE-SEM), atomic force microscopy (AFM), and electrochemical experiments. Galvanostatic charge/discharge measurements indicate that Cu_2O-TiO_2 nanomaterials exhibit very attractive high-rate capabilities (~400 mA h g^{-1} at 1 C; ~325 mA h g^{-1} at 2 C) and good stability after 50 operating cycles, with a retention of 80% of the initial capacity. This phenomenon is mainly due to the presence of TiO_2 acting as a buffer material, i.e., minimizing volume changes occurring in the electrochemical conversion. In a different way, CuO−TiO_2 systems exhibit worse electrochemical performances as a consequence of their porous morphology and higher thickness. In both cases, the obtained values are among the best ever reported for Cu_xO-based systems, candidating the present nanomaterials as extremely promising anodes for eventual applications in thin film lithium batteries.

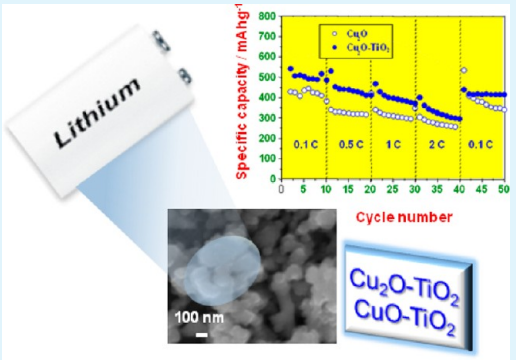

KEYWORDS: *chemical vapor deposition, copper oxides, titanium dioxide, energy storage, thin film lithium batteries*

INTRODUCTION

In the search for high storage capacity and cost-effective anode materials for innovative thin film lithium batteries, transition metal oxides (M_xO_y, with M = Fe, Co, Ni, and Cu) have been widely investigated since they were first proposed by Tarascon et al.[1] In fact, these materials have the ability to reversibly store a high Li amount through a heterogeneous conversion reaction[2−5]

$$2y\mathrm{Li} + \mathrm{M}_x\mathrm{O}_y \rightleftarrows y\mathrm{Li}_2\mathrm{O} + x\mathrm{M} \quad (1)$$

Nevertheless, the application of such oxides is often hindered by their modest electronic conductivity and large volume changes occurring during charge/discharge cycles. In particular, the latter effect might result in M_xO_y pulverization,[6] and subsequent polarization/insulation of the electrode. This issue still needs to be adequately addressed by a suitable choice of active materials and the development of versatile synthetic protocols enabling to tailor the system structural and morphological organization. As a consequence, fundamental research in this field is still necessary and highly demanded.

Among transition metal oxides, Cu_2O and CuO are undoubtedly an attractive choice,[2,5,6] since they are abundant, environmentally benign and inexpensive in comparison to other investigated systems.[7,8] In spite of these advantages, a key challenge for Cu_xO (x = 1, 2) practical use in thin film lithium batteries is the improvement of their high-rate capacity and cycling performances, which are both still far from meeting technological requirements. In this regard, various research efforts have been devoted to the preparation of nanostructured Cu_xO materials with different morphologies (e.g., nanoparticles, nanowires, nanosheets, hollow nanostructures, ...),[2−4,6,9−17] with particular attention to nanocomposites with tailored spatial organization.[5,18−28] Despite improved electrochemical performances having been reported for these systems, thanks to the large active surface area and the decreased diffusion pathway for both electrons and lithium ions,[6,7,29] the charge transfer between copper oxides and current collector is still

Received: April 18, 2012
Accepted: June 15, 2012
Published: June 16, 2012

limited, especially at high cycling rates.[5] In an attempt to solve this problem, powdered Cu_xO were blended with conductive reagents/polymer binders[3,6] to coat the metal collector. Nevertheless, disadvantages related to the poor contact of the latter with the oxide phase, as well as to the formation of additional inactive interfaces between Cu_xO and binders, have still to be fully overcome.[4,5] To this aim, the preparation of supported and nanostructured copper oxides is a valuable option for use in thin film lithium batteries, since the intimate contact with the current collector facilitates electron transfer processes, avoiding the use of any ancillary additive. In this context, a careful control of grain size and film thickness must be properly pursued in order to avoid detrimental alterations of the contact area between Cu_xO particles and the electrolyte,[5] whose diffusion through the film restrains the electrochemical reactivity.

Herein, we present an unprecedented strategy for the preparation of Ti-supported copper oxide-based electrodes for thin film lithium batteries. The proposed strategy consists in the initial chemical vapor deposition (CVD) of Cu_xO nanomaterials starting from $Cu(hfa)_2$·TMEDA (hfa = 1,1,1,5,5,5-hexafluoro-2,4-pentanedionate; TMEDA = *N*,*N*,*N*′,*N*′ - tetramethylethylenediamine). Such a route led to the selective obtainment of Cu_2O or CuO nanomaterials by varying the growth temperature (400, 550 °C) and the operating pressure (3, 10 mbar).[30−33] Beside enabling us to avoid the use of binders and/or ancillary materials,[3,8] this approach resulted in an optimal adhesion between Cu_xO and the used titanium substrate. In a subsequent processing step, the deposition of controlled TiO_2 amounts was performed adopting $Ti(O\text{-}^iPr)_2(dpm)_2$ ($O\text{-}^iPr$ = isopropoxy; dpm = 2,2,6,6-tetramethyl-3,5-heptanedionate) as precursor. The over-dispersion of TiO_2 on copper oxides, reported for the first time in the present work, was aimed at improving the anode electrochemical efficiency.

Notably, the vapor phase strategy proposed herein enabled a simultaneous tailoring of the system phase composition and nano-organization, with an intimate contact between Cu_xO and TiO_2. These features synergistically contributed to the attractive electrochemical behavior observed for the assembled electrodes, in terms of both specific capacities and cycling performances.

To date, only a few works on Cu/TiO_2 nanocomposites for such applications are available in the literature, dealing with the use of copper-containing particles as intermixed current collectors to improve TiO_2 electrochemical performance.[7,29,30] The proposed synthesis involved the slurry casting of powdered materials onto the current collectors after mixing with conductive additives, whose use can be conveniently avoided by the present synthetic strategy.[7,29] Though representing a fundamental study, the results obtained in this work can provide a valuable guidance in view of further optimization of standard batteries.

EXPERIMENTAL SECTION

Synthesis. Copper oxide nanostructures were grown by a custom-built cold-wall CVD apparatus consisting of a tubular quartz chamber, a resistively heated susceptor, and an external reservoir for precursor vaporization,[34] adopting $Cu(hfa)_2$·TMEDA as molecular source.[35] On the basis of our recent results,[31,32] the synthesis of pure Cu_2O and CuO nanostructures was performed at temperatures of 400 and 550 °C (deposition time = 2 h; precursor vaporization temperature = 70 °C). Vapor transport toward the deposition zone was performed through heated gas lines (120 °C) by an O_2 flow (purity = 6.0; flow rates = 20 and 100 sccm for Cu_2O and CuO, respectively). In addition, an auxiliary oxygen flow (20 and 100 sccm for the two cases) was introduced separately into the reaction chamber after passing through a water reservoir (50 °C). Total pressures were set at 3.0 and 10.0 mbar for Cu_2O and CuO, respectively, with corresponding estimated H_2O partial pressures of ∼0.3 and 1.5 mbar.[34] Depositions were performed on Ti substrates (99.7%, Aldrich; thickness = 0.25 mm, size = 8 × 8 mm^2), previously subjected to ultrasonic degreasing in dichloromethane, rinsing in isopropanol, and final drying in air.

Subsequent TiO_2 dispersion was performed starting from $Ti(O\text{-}^iPr)_2(dpm)_2$ (99.99%, Aldrich; vaporization temperature = 80 °C) adopting the same CVD equipment, at total pressure of 10.0 mbar and substrate temperature of 400 °C [deposition time = 20 min, 40 and 80 sccm flow rates for the precursor mass-transport (O_2) and the auxiliary inlet (O_2 + H_2O), respectively]. The use of higher temperatures was discarded in order to prevent undesired modifications of Cu_2O and CuO matrices. All the other parameters were set as for the Cu_xO deposition. The obtained Cu_xO-TiO_2 composite samples were cooled down at room temperature before contacting the external atmosphere and subsequently characterized without any ex situ treatment.

Characterization. GIXRD patterns were collected at a constant incidence angle of 1° by a Bruker D8 Advance diffractometer equipped with a Göbel mirror, using a Cu Kα X-ray source powered at 40 kV and 40 mA. Scherrer equation was used to estimate the mean crystallite sizes.

XPS analyses were carried out by a Perkin-Elmer Φ5600ci spectrometer at pressures lower than 10^{-8} mbar, using a non-monochromatized Mg Kα source ($h\nu$ = 1253.6 eV). After a Shirley-type background subtraction, raw spectra were fitted by a least-squares deconvolution, adopting Gaussian−Lorentzian peak shapes. The reported binding energies (BEs; standard deviation = ± 0.2 eV) were corrected for charging effects by assigning to the adventitious C1s line a position of 284.8 eV. The root-mean-square (rms) uncertainty on each concentration value was assumed to be 15%, according to previous literature reports.[36]

Plane-view and cross-sectional FE-SEM images were recorded by a Zeiss SUPRA 40VP, using accelerating voltages between 10 and 20 kV.

AFM characterization was carried out by using a Nanoscope IIIa AFM (Digital Instruments) operated in contact mode, employing SiN cantilevers (Veeco) with a spring constant of 0.73 N m^{-1}. rms roughness values were calculated from the height profile of 2 × 2 μm^2 micrographs.

SIMS measurements were carried out by means of a IMS 4f mass spectrometer (Cameca), using a Cs^+ primary beam (14.5 keV, 12 nA) and negative secondary ion detection. The charge build up upon profiling was compensated by an electron gun. The signals were recorded in beam blanking mode in order to improve the in-depth resolution. Analyses were performed on 5 different sample regions in order to check the system homogeneity. The erosion speed was evaluated at the end of each analysis by measuring the crater depth through a Tencor Alpha Step profilometer (resolution close to 1 nm), and deposit thickness values were thus obtained. To avoid mass interference artifacts, measurements were performed in high mass resolution configuration. Data in Figure 3 have been plotted without taking into account the sputtering yield dependence on the local composition.

Electrochemical Measurements. Electrochemical tests were performed in two electrode Swagelok-type cells, using lithium as a counter electrode and a Merck battery electrolyte LP 40 [ethylene carbonate (EC) - diethyl carbonate (DEC), EC/DEC = 1:1 w/w, 1 M $LiPF_6$]. Titanium pieces coated with the active nanomaterials were used as working electrodes. The oxide amount on each sample was determined by weighing the Ti substrate before and after deposition on a Sartorius microbalance (sensitivity = ± 1 μg). For the Faradic yield calculation, the TiO_2 amount was considered negligible. Cells were galvanostatically charged and discharged at different cycling rates, from 0.1 to 2 C (C was defined as 375 and 674 mA h g^{-1} for Cu_2O and CuO samples, respectively). The electrodes were first discharged and, subsequently, maintained at their open circuit voltage in order to analyze the electrochemical impedance. After this procedure, the first

charge curve started at potentials higher than 1.0 V. Measurements were controlled via a MacPile potentiostat-galvanostat.

Electrochemical impedance spectroscopy (EIS) analyses (frequency range = 1×10^{-5} to 90 kHz, amplitude = 3 mV) were performed by means of a Solartron 1470 battery test unit coupled to a Schlumberger SI 1255 response analyzer, on the same electrode at different stages during the cycling test.

RESULTS AND DISCUSSION

Chemical and Physical Characterization. GIXRD patterns of Cu_xO-TiO_2 composites, together with those of the corresponding bare Cu_xO systems, are displayed in Figure 1. For Cu_2O-TiO_2, only signals related to the Cu_2O crystalline

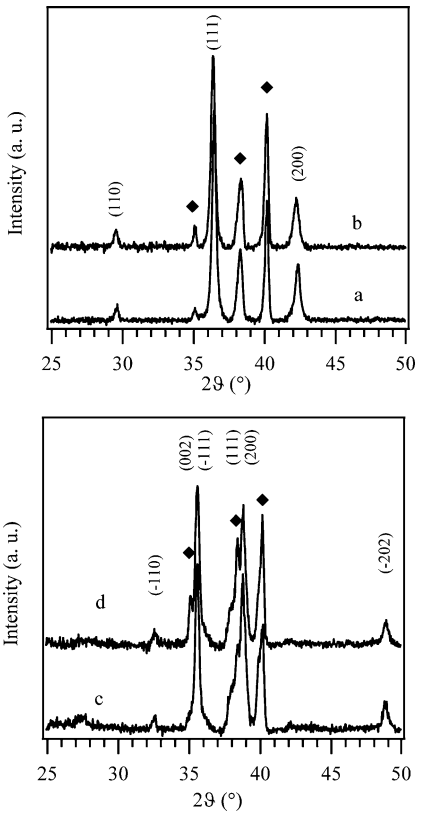

Figure 1. GIXRD patterns of: (a) Cu_2O, (b) Cu_2O-TiO_2, (c) CuO, (d) CuO-TiO_2 samples. Peaks located at 2θ = 35.1, 38.4, and 40.2° (♦) are due to the titanium substrate.

phase (cuprite) could be observed (2θ = 29.6, 36.4, and 42.3°).[37] In the case of CuO-TiO_2, GIXRD patterns were dominated by CuO (tenorite) reflections (2θ = 32.5, 35.5, 38.7, and 48.8°).[38] Regardless of the preparation conditions, no peaks corresponding to crystalline TiO_2 or to Cu−Ti−O ternary phases were present because of the high titania dispersion and moderate amount.[32] These observations highlighted the selective obtainment of Cu_2O- and CuO-based materials by a proper choice of the substrate temperature (400 and 550 °C) and of the total operating pressure (3.0 and 10.0 mbar). For both copper oxide phases, the average crystallite size was estimated to be 30 ± 5 nm, regardless of TiO_2 presence.

To attain a deeper insight into the chemical composition, the nanosystems were characterized by XPS surface analysis (see Figure 2). The mean Ti2$p_{3/2}$ BE (458.6 eV, Figure 2) pointed out to the formation of pure TiO_2,[29,31,32,39−41] excluding the presence of Ti(III) and of any Cu−Ti−O ternary phase. As a

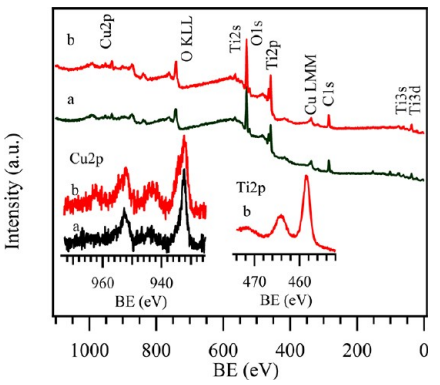

Figure 2. XPS surface survey, along with Cu2p and Ti2p signals, for: (a) Cu_2O-TiO_2, and (b) CuO-TiO_2 nanocomposites.

general rule, copper signals could be observed even after TiO_2 deposition because of the moderate titania content and its dispersion into the underlying matrix (see also SIMS depth profiles, Figure 3). In fact, the process did not produce a complete coverage of the underlying copper oxide matrices under the adopted conditions.

In particular, XPS surface mapping provided the following Cu:Ti atomic percentage ratios (at. %): 18.1:81.9 for Cu_2O-TiO_2, 16.7:83.3 for CuO-TiO_2. In the case of Cu_2O, the presence of Cu(I) was confirmed by the Cu2$p_{3/2}$ peak position (BE = 932.3 eV) and the absence of shake-up satellites.[2,29,39−41]

After TiO_2 deposition, no significant Cu2p spectral change took place, suggesting that the chemical nature of the Cu_2O matrix remained almost unaltered. Regarding CuO specimen, the Cu2$p_{3/2}$ BE (934.0 eV), and the presence of shake-up satellites located at BE ≈ 9.0 eV higher than the related spin−orbit components clearly indicated the occurrence of Cu(II).[4,31,32,41] The subsequent TiO_2 deposition resulted in a partial surface reduction of Cu(II) to Cu(I), as confirmed by: (i) the intensity decrease of shake-up peaks; (ii) the appearance of a Cu2$p_{3/2}$ band at 932.1 eV [assigned to Cu(I)], along with a shoulder located at 934.0 eV [assigned to Cu(II)]. The coexistence of Cu(I)−Cu(II) at the surface could be due to the presence of O-deficient titania particles acting as oxygen getters at the interface with CuO, as already reported.[32,39]

The in-depth penetration of TiO_2 into Cu_xO matrices was investigated by SIMS, and representative profiles are displayed in Figure 3. All specimens presented a homogeneous composition, without any significant carbon contamination, and TiO_2 deposition over Cu_xO matrices resulted in an increase of the overall deposit thickness (Table 1). Notably, an appreciable Cu_xO-TiO_2 intermixing was detected, a phenomenon more evident in the case of CuO-based composites for the synergy between CuO roughness/porosity (see below) and the typical infiltration power of CVD techniques. Such characteristics were responsible for the tailing of copper signals into the substrates themselves. In fact, as can be observed from panels c and d in Figure 3, the deposit-Ti interface was significantly broadened for CuO-based systems. The maximum-like behavior in the Ti profile at the interface with the substrate, particularly evident in the case of Figure 3a, was due to the SIMS yield dependence on the sputtering yield coefficient, which in turn is a function of the matrix composition. This dependence implies that the same element (e.g., Ti) can have different yields upon passing from the target material to the substrate.

dx.doi.org/10.1021/am300678t | ACS Appl. Mater. Interfaces 2012, 4, 3610−3619

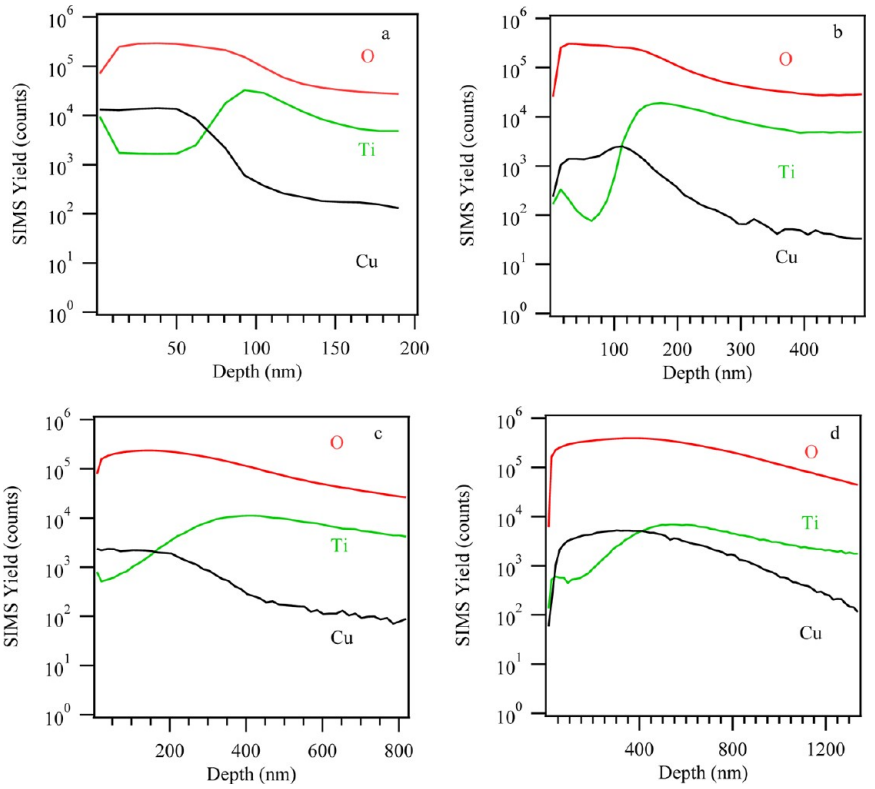

Figure 3. Representative SIMS depth profiles for: (a) Cu_2O, (b) Cu_2O-TiO_2, (c) CuO, (d) CuO-TiO_2 nanocomposites.

Table 1. RMS Surface Roughness and Nanodeposit Thickness for Cu_xO-TiO_2 Nanocomposites

rms roughness (nm)	thickness (nm)	sample
30 ± 2	85 ± 15	Cu_2O
30 ± 2	134 ± 20	Cu_2O-TiO_2
70 ± 3	275 ± 55	CuO
140 ± 5	325 ± 85	CuO-TiO_2

FE-SEM and AFM micrographs (Figure 4) revealed that the different synthesis conditions used for Cu_2O and CuO depositions had a significant influence even on the system nanoscale organization. For the thinnest Cu_2O-based specimens, the morphology was mainly dominated by the typical corrugation of Ti substrate. In fact, as can be observed, a uniform conformal coverage of the latter by rounded Cu_2O nanoaggregates (mean dimensions = 100 ± 20 nm) took place, suggesting an isotropic growth mode. The subsequent TiO_2 deposition induced a mean nanoaggregate size increase of 30 nm, due to the deposition of TiO_2 particles on Cu_2O grains (see Figure S1 in the Supporting Information). Conversely, the morphology of CuO-based nanosystems was characterized by the presence of interwoven aggregates, resulting in a highly porous deposit. The observed features had mean lateral sizes of 450 ± 50 nm and were formed by the agglomeration of smaller grains (150 ± 30 nm). Such values were higher than the crystallite sizes calculated by GIXRD data, suggesting that the observed particles were formed by the aggregation of various crystalline domains. Even in this case, titania deposition did not appreciably alter the pristine morphology of the bare CuO matrix, but induced only a mean increase of the lateral dimensions (200 and 50 nm for the above-mentioned interwoven aggregates and grains, respectively). Overall, these observations underlined the occurrence of a high TiO_2 dispersion into the CuO matrix, with an intimate contact between the two oxides.

The surface rms roughness values obtained by AFM analyses are reported in Table 1. Note that after titania dispersion, no change occurred in the rms roughness values for Cu_2O-based systems, highlighting a conformal coverage of the copper(I) oxide matrix. Conversely, CuO samples were appreciably rougher, and their coverage by TiO_2 resulted in a significant roughness increase. In the case of such systems, the high rms roughness was responsible for the appearance of flat-wall aggregates in AFM images, since these were not properly accessible to the AFM tip (see Figure 4c, d). The higher rms roughness values for CuO-based systems were indicative of a larger active area,[8] anticipating thus appreciable differences in the electrochemical behavior of Cu_2O- and CuO-based nanocomposites.

Electrochemical Characterization. To test the applicability of the present systems as anodes in thin film batteries, their properties with respect to Li insertion/extraction were investigated. The galvanostatic charge/discharge curves recorded during the first three cycles for Li/Cu_xO and Li/Cu_xO-TiO_2 cells are displayed in Figure 5. The voltage profiles are similar to those already described for Cu_2O[25] and CuO[12,22,42] electrodes and consistent with the following half-reactions[1,2,43]

$$Cu_2O + 2Li^+ + 2e^- \rightleftarrows 2Cu + Li_2O \quad (2)$$

$$CuO + 2Li^+ + 2e^- \rightleftarrows Cu + Li_2O \quad (3)$$

Upon discharging, Cu_xO were transformed into nanometric Cu particles. After the first discharge cycle, the electrode Faradic yield exceeded the stoichiometric value for two electrons, a phenomenon which could be related to the formation of a solid electrolyte interphase (SEI) layer.[8,44,45] The presence of the

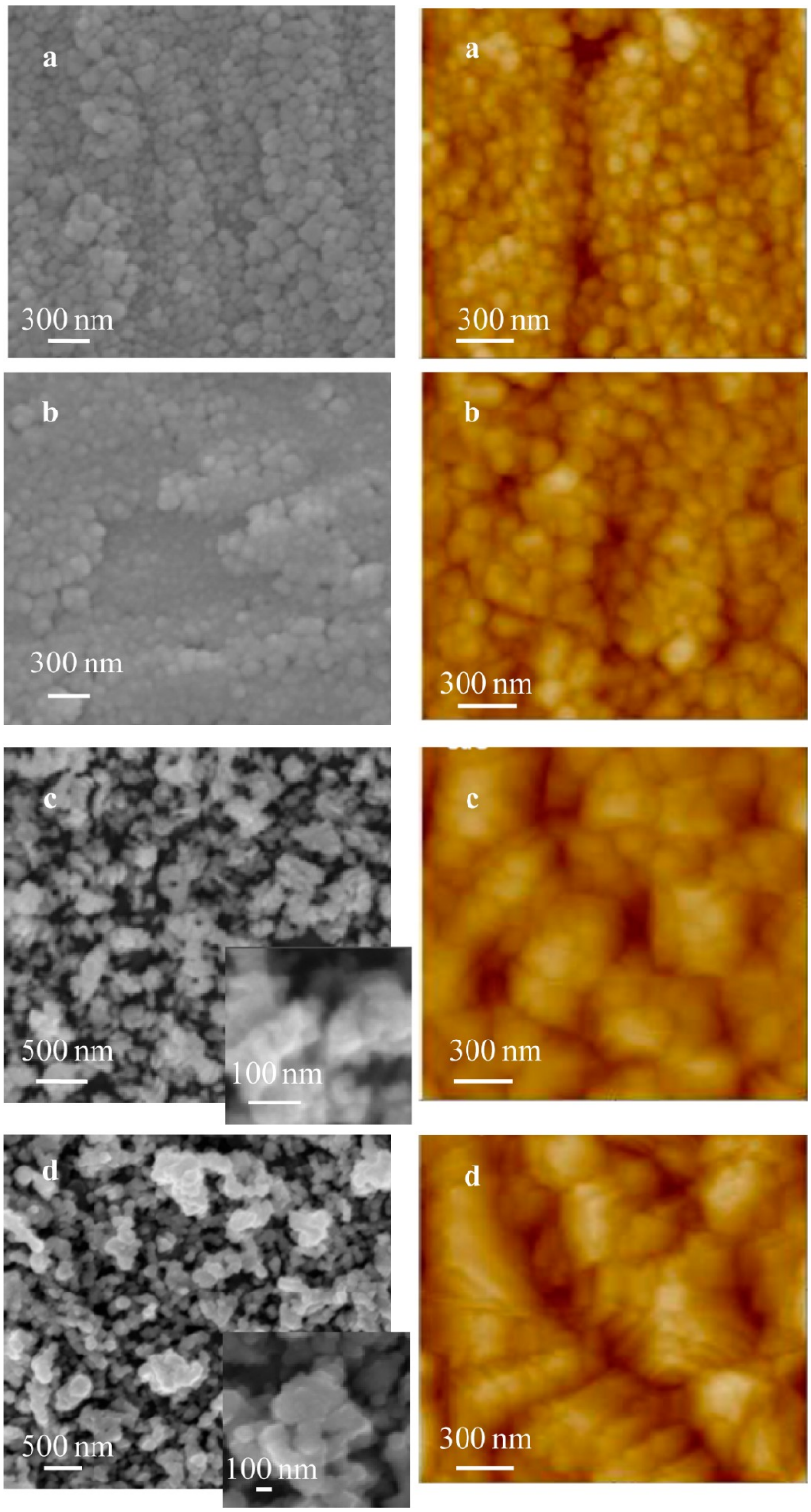

Figure 4. FE-SEM and AFM micrographs of: (a) Cu_2O, (b) Cu_2O-TiO_2, (c) CuO, (d) CuO-TiO_2.

latter was ascribed to the catalytic activity of metal particles, which can activate solvent molecules facilitating the charge transfer needed for redox processes.[45] Such a phenomenon explains why approximately twice the reversible capacity calculated for the samples was obtained at 0.1 C rate (compare Figure 6 and comments below). Notably, regardless of copper oxide nature, the dispersion of TiO_2 increased the capacity delivered by the electrodes.

As a matter of fact, the exceeding Faradic yield value measured for each electrode was directly correlated with its microstructure and morphology, since electrodes exhibiting a larger interfacial area with the electrolyte facilitated its reduction and the SEI layer formation.[4] This phenomenon was more evident for CuO and TiO_2-covered electrodes because of the synergistic contribution of the following factors: (i) CuO deposits were very porous and characterized by higher

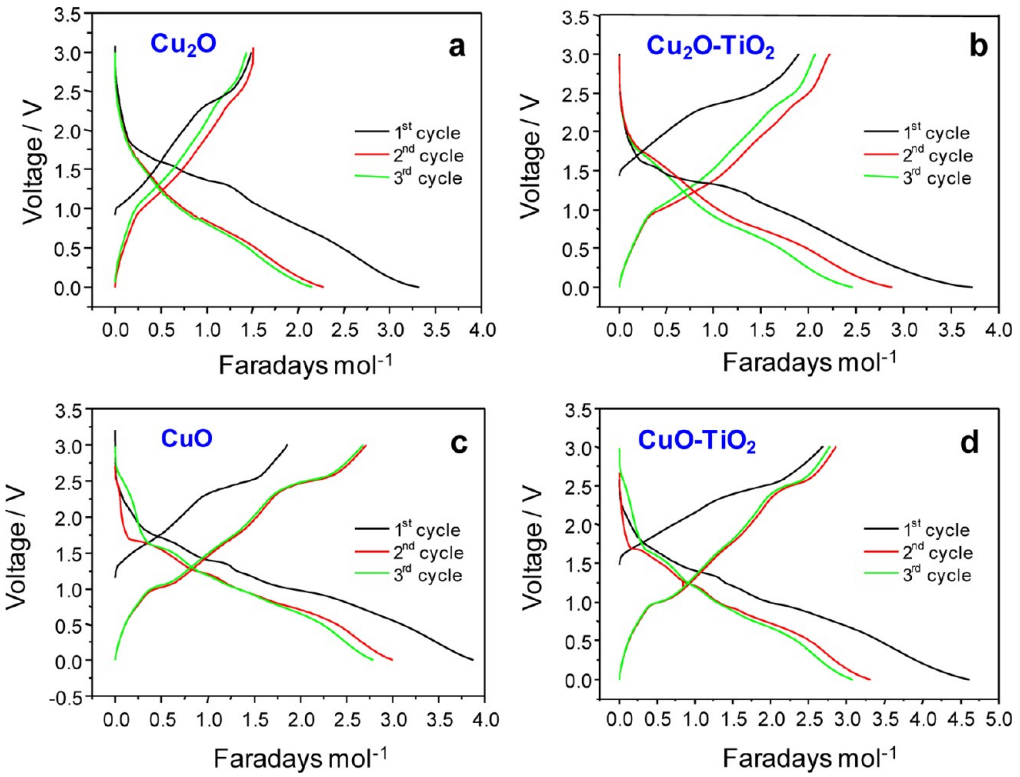

Figure 5. Charge/discharge voltage profiles during the first three operational cycles for: (a) Cu_2O, (b) Cu_2O-TiO_2, (c) CuO, (d) CuO-TiO_2 specimens, cycled between 3.0 and 0.0 V (vs. Li^+/Li).

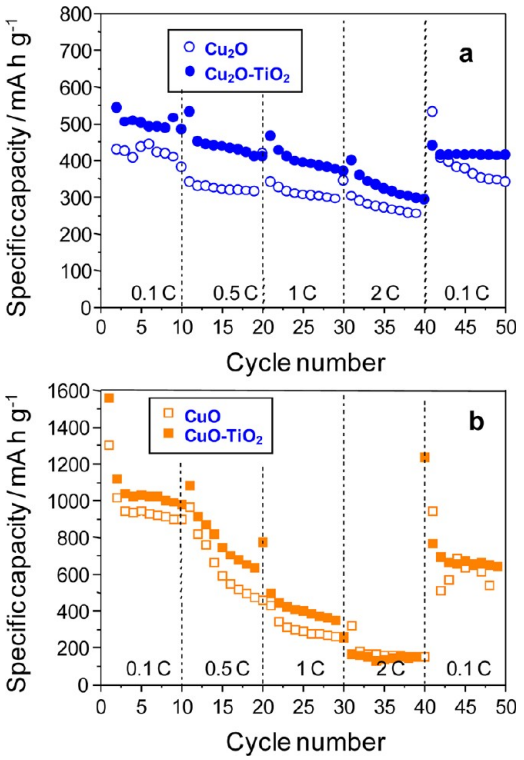

Figure 6. Comparison of the rate capabilities as a function of cycle number for the different nanocomposite electrodes. Voltage limits are between 3.0 and 0.0 V (vs. Li^+/Li).

rms values than the more compact Cu_2O ones (compare Figure 3 and Table 1); (ii) the coverage of Cu_xO nanoaggregates by TiO_2 produced an increase of their mean size and/or roughness (Table 1). The electricity amount involved in the first discharge was only partially extracted in the subsequent charging process, suggesting thus the occurrence of an incomplete Li_2O/SEI decomposition.[8] Nevertheless, under the 0.1 C regime, the SEI layer formation progressed and further proceeded during the following cycles, particularly for the CuO-based electrode. As a general trend, the charge/discharge curve shapes were rather similar upon cycling, indicating the occurrence of highly reversible electrochemical processes. No discernible signal was observed at 1.74 V, the voltage value attributed to lithiation/delithiation of TiO_2,[46] in agreement with the moderate content of this oxide.

The specific capacities of the different electrodes cycled in the 3.0−0.0 V range under various C regimes (see the Experimental Section) are reported in Figure 6. At 0.1 C, the delivered values for Cu_2O and CuO samples were larger than the expected theoretical ones (375 and 674 mA h g^{-1}, respectively),[2−4] indicating the electrolyte participation to the cycling process,[8] as also supported by ex situ FE-SEM observations (Figure 8b). This phenomenon was more important at low C regimes (0.1 C), altering the observed cycle stability. The capacity evolution upon increasing the charging/discharging rate from 0.1 to 2 C was significantly influenced by the electrode microstructure and morphology. As a matter of fact, CuO and CuO-TiO_2 samples, constituted by bigger nanoaggregates forming thicker and highly porous deposits (see rms roughness values in Table 1), exhibited limited capacity retention upon faster cycling. Conversely, the more compact and thinner Cu_2O and Cu_2O-TiO_2 deposits possessed good cycling electrochemical performances and a maximum capacity loss of 35% was observed in the fastest regime (2 C). High capacity values were recovered when Cu_2O-based electrodes were charged/discharged again at 0.1 C after

dx.doi.org/10.1021/am300678t | ACS Appl. Mater. Interfaces 2012, 4, 3610−3619

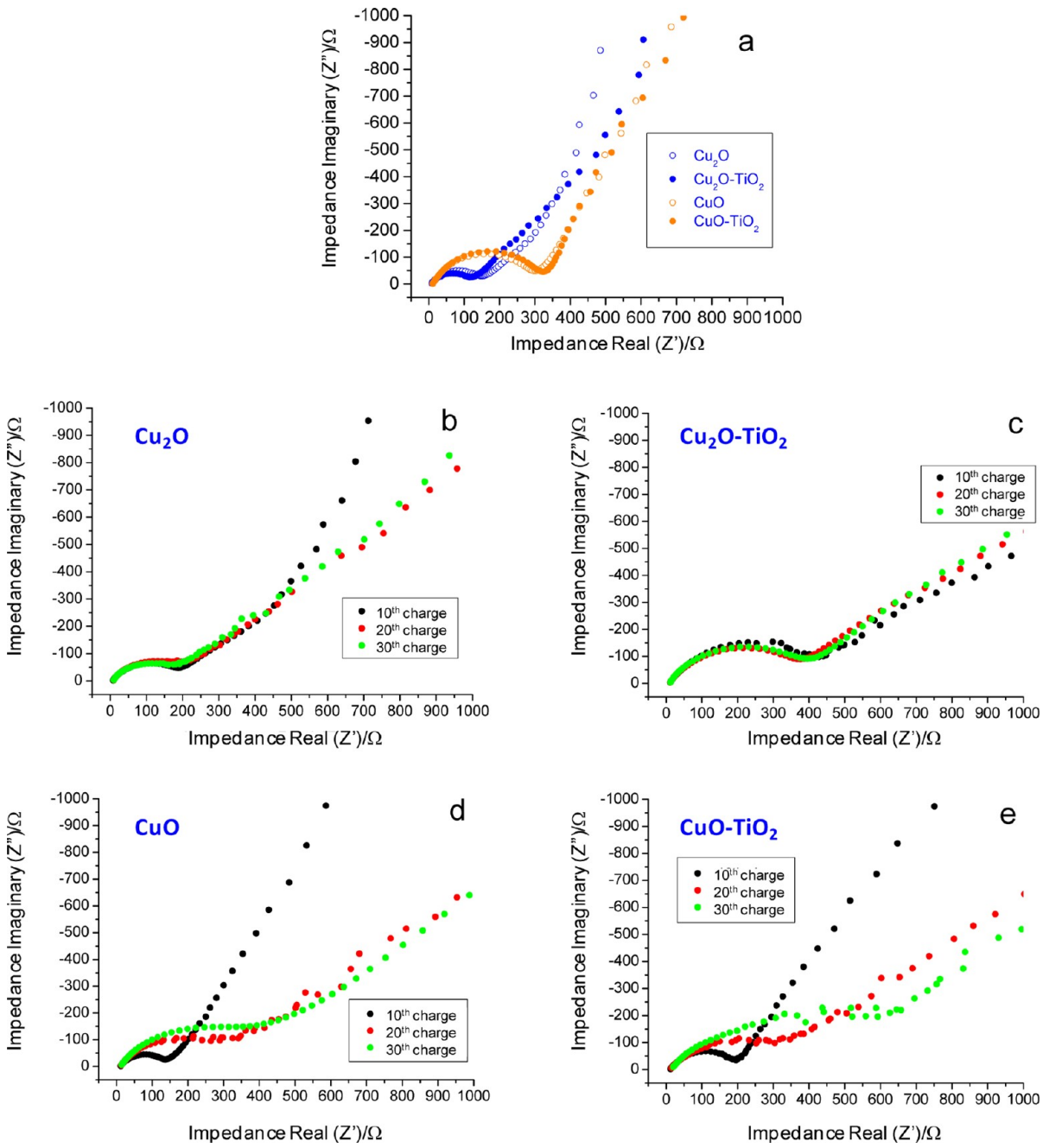

Figure 7. (a) EIS spectra for electrodes in the discharged state at 0.0 V. EIS spectra for: (b) Cu_2O, (c) Cu_2O-TiO_2, (d) CuO, (e) CuO-TiO_2 electrodes in the charged state at 3.0 V, after various cycles.

40 cycles, reaching 80% of the original values. For Cu_2O-TiO_2 systems (Figure 6a), upon returning to the 0.1 C regime after 40 cycles, an improved cycle stability with respect to the first 10 cycles was observed. This effect was traced back to a decreased electrolyte participation to the electrochemical process. Consistently, after 40 cycles, the delivered capacity (~400 mA h g^{-1}) could be mainly ascribed to the reversible $Cu_2O \rightleftarrows Cu$ reaction, in agreement with the observed cycle stability.

The deposition of TiO_2 had minor influence on the sample rate capability. For instance, Cu_2O samples retained 95 and 90% of the initial capacity when the operating regime was changed from 0.5 to 2 C (average capacity values: 320, 305, and 272 mA h g^{-1} at 0.5, 1, and 2 C, respectively). In a different way, for Cu_2O-TiO_2 sample the corresponding capacity retention was lower, 91 and 81% (436, 396, and 324 mA h g^{-1} at 0.5, 1, and 2 C, respectively). The worse rate capability of TiO_2-containing samples is in line with their larger impedance, as indicated by EIS analysis (see Figure 7 and related comments). It is also worth mentioning that all electrodes maintained values close to their theoretical capacity after cycling experiments.

To the best of our knowledge, the capacity values measured for both Cu_xO-TiO_2 systems are among the best ever reported to date for Cu_2O and CuO (see Table S1 in the Supporting Information),[3,5,11,15,16,18,22,47] demonstrating the technological potential of the adopted synthesis procedure. The worse electrochemical behavior of CuO-based electrodes could be explained on the basis of their morphology and thickness. As

already discussed, their porosity, resulting in a higher interfacial area with the electrolyte than for Cu_2O-based systems, facilitated the formation of a SEI polymeric film embedding CuO-containing particles, restricting, in turn, Li^+ diffusion through the active material. In addition, the electrochemical performances of copper oxide films were strongly dependent on thickness, indicating that the electron transfer from the Ti substrate through the whole nanodeposit directly influenced the electrochemical process kinetics.[48] Thus, during the charging process, when the metallic substrate acted as electron drain, the inner deposit layers were the first ones undergoing oxidation and the subsequent electron conduction from the outermost region was limited by the Cu → Cu_xO conversion. This effect was more pronounced for thicker systems, i.e., in the case of CuO-based nanocomposites.

To gain a better understanding of the system electrochemical behavior, a combined FE-SEM and EIS characterization was undertaken on the discharged electrodes. Figure 7a displays EIS spectra after the first discharge at 0.0 V. For all measurements, the Nyquist plots showed the characteristic depressed semicircle in the high- and middle-frequency range, followed by a straight line in the middle- to low-frequency range. As previously reported for Cu_2O and CuO electrodes,[5,11] only one semicircle was observed, which is considered to arise from the superimposition of two separate contributions at high and medium frequencies. Whereas the former could be attributed to a polymerlike SEI film and/or contact resistance, the latter was related to Li^+ charge transfer impedance at the electrode/electrolyte interface.[8]

At 0.0 V, both Cu_2O-based electrodes show a smaller high-medium frequency semicircle than CuO-containing ones, indicating that both lithium ions and electrons could be transferred more easily across the Cu_2O/electrolyte interface. This observation was in agreement with data of Figure 5, showing that the formation of a passive SEI film during the first discharge was favored for CuO-based systems. Upon cycling, impedance spectra were recorded at the end of the 10th, 20th and 30th charge process performed at 0.1, 0.5, and 1 C regimes, respectively. Even though the semicircle was extended to lower frequencies in the case of Cu_2O and Cu_2O-TiO_2 electrodes (Figure 7b, c), the Nyquist plot shapes did not significantly change, suggesting that both the electrode microstructure and the mobility of Li^+ and e^- did not undergo significant variations during cycling. In a different way, in the case of CuO and CuO-TiO_2, the semicircle became more extended upon increasing the cycle number (Figure 7d, e), indicating a progressive growth of the SEI film and explaining the inferior electrochemical performance of these electrodes under high charge/discharge regimes.

For both Cu_2O- and CuO-based systems, TiO_2 introduction resulted in an impedance increase with respect to the bare Cu_xO matrices, that could be traced back to: (i) a favored electrolyte degradation and formation of SEI film;[49] (ii) a limited electron transfer, due to the poor titania electron conduction. On the other hand, it is worth noting that this phenomenon is not a handicap in order to achieve an optimal electrochemical behavior, as observed in the case of Cu_2O-TiO_2.

Figure 8 shows the FE-SEM images recorded after electrochemical tests, which revealed the occurrence of various changes with respect to the as-grown systems (Figure 4). For Cu_2O and Cu_2O-TiO_2, a compact morphology was present and the pristine nanoparticulate features could no more be discerned. The development of cracks on Cu_2O (Figure 8a, inset), which could limit the electron conduction through the electrode, was induced by the volume variations experienced upon electrochemical cycling.[4,6,8,15] In addition, the Cu_2O electrode was completely covered by a jelly film (Figure 8a). Significant alterations were observed for Cu_2O-TiO_2 (Figure 8b), namely: (i) large aggregates appeared on the electrode surface, likely attributable to electrolyte degradation products; (ii) no jelly film could be observed (see also below); (iii) no cracks could be clearly detected. The fact that TiO_2 particles covered the Cu_2O matrix, as inferred from XPS, SIMS and AFM data, evidenced titania role as buffer material, preserving the system structure upon cycling.[50] Conversely, CuO and CuO-TiO_2 exhibited similar aggregate sizes and their pristine porous topography appeared to be filled by a polymeric material (Figure 8c, d), further supporting the promotional effect of this peculiar morphology on the formation of the SEI layer, which worsened the system electrochemical performances.

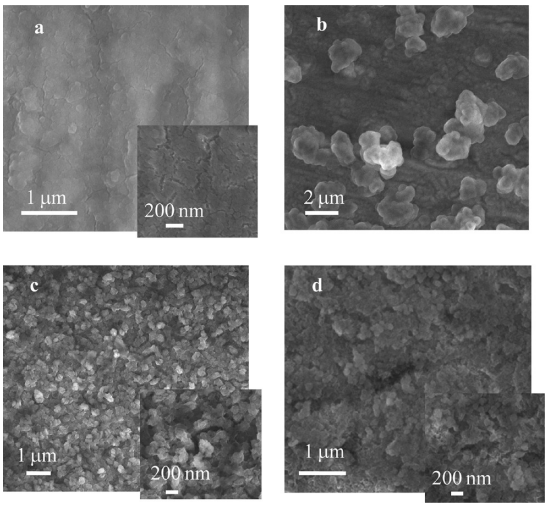

Figure 8. FE-SEM images of: (a) Cu_2O, (b) Cu_2O-TiO_2, (c) CuO, (d) CuO-TiO_2 electrodes, recorded after the cycling tests.

The role of TiO_2 on the electrochemical performances of copper oxide electrodes can be explained in detail considering Cu_2O-containing systems as an example. On the basis of SIMS results, TiO_2 was located not only in the outermost system region but also in the inner one. The surface presence of titania enhances the SEI film formation because of TiO_2 activity in the electrochemical electrolyte degradation,[49] resulting in the observed capacity excess upon discharging TiO_2-containing electrodes. This behavior, together with the poor titania conductivity, precludes a fast transfer of both lithium ions and electrons through the copper oxide matrix, deteriorating the rate capability of Cu_xO-TiO_2 electrodes.

This detrimental titania contribution is counterbalanced by its beneficial influence on the delivered electrode capacity, a phenomenon occurring irrespective of copper oxide nature, that can be traced back to the concurrence of two main causes. The first one is the buffering effect exerted by Cu_xO-TiO_2 intermixing, lowering, in turn, volume changes occurring during reactions (2) and (3) with respect to the bare Cu_xO systems. Such an explanation is perfectly in line with observations on the lithium insertion/extraction process for ZnO nanorods functionalized with TiO_2 nanoparticles.[50] No cracks, whose formation would be a handicap for electron conduction, were

observed on Cu_xO-TiO_2 electrodes, in line with the good capacity retention observed after 40 cycles.

The second cause explaining the increased capacity for Cu_xO-TiO_2 systems is related to the dynamics of SEI layer formation/reoxidation, both being activated by TiO_2 presence. Indeed, as already reported, TiO_2 enhanced the electrochemical reactivity of Fe_2O_3 anodes by promoting the electrolyte redox process.[46] In the present case, the two-fold TiO_2 role is supported by FE-SEM micrographs of panels a and in Figure 8, displaying significant differences between bare Cu_2O and Cu_2O-TiO_2 systems after electrochemical cycling. In fact, a jelly SEI film was observed on the surface of the bare Cu_2O electrode, but not on the Cu_2O-TiO_2 one.

CONCLUSIONS

In summary, we have proposed a successful vapor phase route to develop Cu_xO-TiO_2 (x = 1, 2) nanoelectrodes free from ancillary additives. A suitable choice of the growth temperature and oxygen total pressure enabled the selective preparation of Cu_2O/CuO matrices with tailored nano-organization, over which TiO_2 nanoparticles were subsequently dispersed. As a result, high-purity Cu_xO-TiO_2 (x = 1, 2) nanocomposites with an intimate contact between Cu_xO and TiO_2 were obtained. We also showed that the morphology and nano-organization of Cu_xO-TiO_2 composites had a significant influence on their electrochemical performances as anodes in thin film lithium batteries, resulting in Coulombic efficiencies and rate capabilities among the highest ever reported for Cu_xO-based materials. In the case of CuO-TiO_2, the porous structure promoted the formation of a SEI polymeric film, restricting thus Li^+ diffusion through the active material, while the high deposit thickness constrained the electron transfer. Both effects were responsible for the limited capacity retention at fast regimes. In a different way, as regards Cu_2O-TiO_2 electrodes, enhanced cycling performances were obtained. In this case, the introduction of TiO_2 minimizes the formation of cracks on the electrode surface and promotes the electrochemical redox conversion of the SEI layer.

Overall, these results give clear evidence of the attractive material performances as thin film battery anodes. The most interesting future perspectives for advancements of the present activities will concern the functional validation of Cu_xO-TiO_2 systems after more prolonged electrochemical cycling, an important issue in view of practical technological applications. In addition, the applicability of the present strategy to other nanocomposite oxides will also be investigated, in order to further explore its potential for the development of thin film Li batteries with outstanding efficiency.

ASSOCIATED CONTENT

Supporting Information

Additional figure and table (PDF). This material is available free of charge via the Internet at http://pubs.acs.org.

AUTHOR INFORMATION

Corresponding Author

*E-mail: davide.barreca@unipd.it (D.B.); luis-sanchez@uco.es (L.S.).

Notes

The authors declare no competing financial interest.

ACKNOWLEDGMENTS

We thank the Ministerio de Educación y Ciencia (MEC) (Project MAT2008-03160), Junta de Andalucía (Group 175 and Project P09-FQM-4764), and University of Córdoba for financial support of this work. This work was also funded by the European Community's Seventh Framework Program (FP7/2007-2013; Grant ENHANCE-238409), as well as Padova University PRAT2010 grant (no. CPDA102579). Thanks are due to Mr. A. Ravazzolo and Dr. A. Parfenova (CNR-ISTM and Padova University, Padova, Italy) for technical and synthetic assistance.

REFERENCES

(1) Poizot, P.; Laruelle, S.; Grugeon, S.; Dupont, L.; Tarascon, J. M. *Nature* **2000**, *407*, 496.
(2) Bijani, S.; Gabás, M.; Martínez, L.; Ramos-Barrado, J. R.; Morales, J.; Sánchez, L. *Thin Solid Films* **2007**, *515*, 5505.
(3) Wang, H.; Pan, Q.; Zhao, J.; Yin, G.; Zuo, P. *J. Power Sources* **2007**, *167*, 206.
(4) Morales, J.; Sánchez, L.; Martín, F.; Ramos-Barrado, J. R.; Sánchez, M. *Thin Solid Films* **2005**, *474*, 133.
(5) Pan, Q.; Jin, H.; Wang, H.; Yin, G. *Electrochim. Acta* **2007**, *53*, 951.
(6) Guan, X.; Li, L.; Li, G.; Fu, Z.; Zheng, J.; Yan, T. *J. Alloys Compd.* **2011**, *509*, 3367.
(7) Cao, F.-F.; Xin, S.; Guo, Y.-G.; Wan, L.-J. *Phys. Chem. Chem. Phys.* **2011**, *13*, 2014.
(8) Barreca, D.; Cruz-Yusta, M.; Gasparotto, A.; Maccato, C.; Morales, J.; Pozza, A.; Sada, C.; Sánchez, L.; Tondello, E. *J. Phys. Chem. C* **2010**, *114*, 10054.
(9) Zhang, C. Q.; Tu, J. P.; Huang, X. H.; Yuan, Y. F.; Chen, X. T.; Mao, F. *J. Alloys Compd.* **2007**, *441*, 52.
(10) Xiang, J. Y.; Tu, J. P.; Zhang, L.; Zhou, Y.; Wang, X. L.; Shi, S. J. *J. Power Sources* **2010**, *195*, 313.
(11) Xiang, J. Y.; Wang, X. L.; Xia, X. H.; Zhang, L.; Zhou, Y.; Shi, S. J.; Tu, J. P. *Electrochim. Acta* **2010**, *55*, 4921.
(12) Morales, J.; Sánchez, L.; Martín, F.; Ramos-Barrado, J. R.; Sánchez, M. *Electrochim. Acta* **2004**, *49*, 4589.
(13) Lee, Y. H.; Leu, I. C.; Liao, C. L.; Chang, S. T.; Wu, M. T.; Yen, J. H.; Fung, K. Z. *Electrochem. Solid State Lett.* **2006**, *9*, A207.
(14) Yu, Y.; Shi, Y.; Chen, C.-H.; Wang, C. *J. Phys. Chem. C* **2008**, *112*, 4176.
(15) Feng, J. K.; Xia, H.; Lai, M. O.; Lu, L. *Mater. Res. Bull.* **2011**, *46*, 424.
(16) Ke, F. -S.; Huang, L.; Wei, G.-Z.; Xue, L.-J.; Li, J.-T.; Zhang, B.; Chen, S.-R.; Fan, X.-Y.; Sun, S.-G. *Electrochim. Acta* **2009**, *54*, 5825.
(17) Dar, M.; Nam, S.; Kim, Y.; Kim, W. *J. Solid State Electrochem.* **2010**, *14*, 1719.
(18) Yan, Y.; Shi, Y.; Chen, C.-H. *Nanotechnol.* **2007**, *18*, 055706.
(19) Xiang, J. Y.; Tu, J. P.; Yuan, Y. F.; Huang, X. H.; Zhou, Y.; Zhang, L. *Electrochem. Commun.* **2009**, *11*, 262.
(20) Venkatachalam, S.; Zhu, H.; Masarapu, C.; Hung, K.; Liu, Z.; Suenaga, K.; Wei, B. *ACS Nano* **2009**, *3*, 2177.
(21) Li, T.; Ai, X. P.; Yang, H. X. *J. Phys. Chem. C* **2011**, *115*, 6167.
(22) Pan, Q.; Wang, M.; Wang, Z. *Electrochem. Solid-State Lett.* **2009**, *12*, A50.
(23) Zhang, X.; Zhang, D.; Ni, X.; Song, J.; Zheng, H. *J. Nanopart. Res.* **2008**, *10*, 839.
(24) Park, J. C.; Kim, J.; Kwon, H.; Song, H. *Adv. Mater.* **2009**, *21*, 803.
(25) Morales, J.; Sánchez, L.; Bijani, S.; Martínez, L.; Gabás, M.; Ramos-Barrado, J. R. *Electrochem. Solid-State Lett.* **2005**, *8*, A159.
(26) Souza, E. A.; Landers, R.; Cardoso, L. P.; Cruz, T. G. S.; Tabacniks, M. H.; Gorenstein, A. *J. Power Sources* **2006**, *155*, 358.
(27) Xiang, J.; Tu, J.; Huang, X.; Yang, Y. *J. Solid-State Electrochem.* **2008**, *12*, 941.

(28) Pan, Q.; Wang, M.; Wang, H.; Zhao, J.; Yin, G. *Electrochim. Acta* **2008**, *54*, 197.
(29) Mancini, M.; Kubiak, P.; Wohlfahrt-Mehrens, M.; Marassi, R. *J. Electrochem. Soc.* **2010**, *157*, A164.
(30) Mancini, M.; Kubiak, P.; Geserick, J.; Marassi, R.; Hüsing, N.; Wohlfahrt-Mehrens, M. *J. Power Sources* **2009**, *189*, 585.
(31) Barreca, D.; Carraro, G.; Comini, E.; Gasparotto, A.; Maccato, C.; Sada, C.; Sberveglieri, G.; Tondello, E. *J. Phys. Chem. C* **2011**, *115*, 10510.
(32) Barreca, D.; Carraro, G.; Gasparotto, A.; Maccato, C.; Lebedev, O. I.; Parfenova, A.; Turner, S.; Tondello, E.; Van Tendeloo, G. *Langmuir* **2011**, *27*, 6409.
(33) Barreca, D.; Carraro, G.; Gombac, V.; Gasparotto, A.; Maccato, C.; Fornasiero, P.; Tondello, E. *Adv. Funct. Mater.* **2011**, *21*, 2611.
(34) Barreca, D.; Gasparotto, A.; Lebedev, O. I.; Maccato, C.; Pozza, A.; Tondello, E.; Turner, S.; Van Tendeloo, G. *CrystEngComm* **2010**, *12*, 2185.
(35) Bandoli, G.; Barreca, D.; Gasparotto, A.; Seraglia, R.; Tondello, E.; Devi, A.; Fischer, R. A.; Winter, M.; Fois, E.; Gamba, A.; Tabacchi, G. *Phys. Chem. Chem. Phys.* **2009**, *11*, 5998.
(36) Briggs, D.; Seah, M. P. *Practical Surface Analysis*, 2nd ed.; John Wiley and Sons: New York, 1990.
(37) JCPDS, pattern no. 5−667, 2000.
(38) JCPDS, pattern no. 45−937, 2000.
(39) Barreca, D.; Carraro, G.; Gasparotto, A. *Surf. Sci. Spectra* **2009**, *16*, 1.
(40) Moulder, J. F.; Stickle, W. F.; Sobol, P. E.; Bomben, K. D. *Handbook of X-ray Photoelectron Spectroscopy*; Perkin-Elmer: Eden Praire, MN, 1992.
(41) *X-ray Photoelectron Spectroscopy (XPS) Database*, version 3.5; National Institute of Standards and Technology: Gaithersburg, MD; (http://srdata.nist.gov/xps/).
(42) Chen, L. B.; Lu, N.; Xu, C. M.; Yu, H. C.; Wang, T. H. *Electrochim. Acta* **2009**, *54*, 4198.
(43) Grugeon, S.; Laruelle, S.; Herrera-Urbina, R.; Dupont, L.; Poizot, P.; Tarascon, J. M. *J. Electrochem. Soc.* **2001**, *148*, A285.
(44) Debart, A.; Dupont, L.; Poizot, P.; Leriche, J. B.; Tarascon, J. M. *J. Electrochem. Soc.* **2001**, *148*, A1266.
(45) Laik, B.; Poizot, P.; Tarascon, J. M. *J. Electrochem. Soc.* **2002**, *149*, A251.
(46) Morales, J.; Sánchez, L.; Martín, F.; Berry, F.; Ren, X. *J. Electrochem. Soc.* **2005**, *152*, A1748.
(47) Zhang, W.; Li, M.; Wang, Q.; Chen, G.; Kong, M.; Yang, Z.; Mann, S. *Adv. Funct. Mater.* **2011**, *21*, 3516.
(48) Bijani, S.; Gabás, M.; Subias, G.; Garcia, J.; Sánchez, L.; Morales, J.; Martínez, L.; Ramos-Barrado, J. R. *J. Mater. Chem.* **2011**, *21*, 5368.
(49) Chang, H.-H.; Chang, C.-C.; Su, C.-Y.; Wu, H.-C.; Yang, M.-H.; Wu, N.-L. *J. Power Sources* **2008**, *185*, 466.
(50) Lee, J.-H.; Hon, M.-H.; Chung, Y.-W.; Leu, I.-C. *Appl. Phys. A: Mater. Sci. Process.* **2011**, *102*, 545.